processes

MDPI

Article

Optimal Design of a Renewable-Energy-Driven Integrated Cooling–Freshwater Cogeneration System

Iman Janghorban Esfahani [1,2,*] and Pouya Ifaei [3,*]

[1] Glopex Co., Ltd., R&D Center, GeumGang Penterium, A2801 IX Tower, 27, Dongtancheomdansaneop 1-ro, Hwaseong-si 18469, Republic of Korea
[2] Regenerative Medicine Laboratory, Center for Stem Cell Research Department of Biomedical Science and Technology, Institute of Biomedical Science and Technology, Konkuk University, Seoul 05029, Republic of Korea
[3] Department of Chemical Engineering and Materials Science, Ewha Womans University, Seoul 03760, Republic of Korea
* Correspondence: john@glopex.kr (I.J.E.); pouya.ifaei@ewha.ac.kr (P.I.); Tel.: +82-2-32774202 (P.I.)

Abstract: This study presents a novel approach that will address escalating demands for water and cooling in regions vulnerable to climate change through the proposal of an optimal integrated cooling–freshwater cogeneration system powered by renewable energy sources. Comprising three subsystems (integrated multi-effect evaporation distillation, absorption heat pump, and vapor compression refrigeration (MAV); renewable energy unit incorporating solar panels, wind turbines, batteries, and hydrogen facilities (RHP/BH); and combined heat and power (CHP)), the system aims to produce both cooling and freshwater. By recovering cooling from combined desalination and refrigeration subsystems to chill the air taken into the gas turbine compressor, the system maximizes efficiency. Through the recovery of waste heat and employing an integrated thermo-environ-economic framework, a novel objective function, termed modified total annual cost (MTAC), is introduced for optimization. Using a genetic algorithm, parametric iterative optimization minimizes the MTAC. The results reveal that under optimum conditions, the MAV, RHP/BH, and CHP subsystems account for 67%, 58%, and 100% of total annual, exergy destruction, and environmental costs, respectively. Notably, the system exhibits lower sensitivity to fuel prices than renewable energy sources, suggesting a need for future research that will incorporate dynamic product prices and greater fuel consumption to produce enhanced operational robustness.

Keywords: cooling–freshwater cogeneration; hydrogen facilities; optimal integrated system; renewable energies; seawater desalination; sensitivity analysis

check for updates

Citation: Janghorban Esfahani, I.; Ifaei, P. Optimal Design of a Renewable-Energy-Driven Integrated Cooling–Freshwater Cogeneration System. *Processes* **2024**, *12*, 1164. https://doi.org/10.3390/pr12061164

Academic Editors: George J. Tsekouras and Fotios D. Kanellos

Received: 13 April 2024
Revised: 1 June 2024
Accepted: 4 June 2024
Published: 5 June 2024

Copyright: © 2024 by the authors. Licensee MDPI, Basel, Switzerland. This article is an open access article distributed under the terms and conditions of the Creative Commons Attribution (CC BY) license (https://creativecommons.org/licenses/by/4.0/).

1. Introduction

One of the severe impacts of climate change is the alteration of precipitation patterns, leading to changes in land use, increased occurrences of floods, and intensified droughts. These changes pose a significant threat to human populations, particularly in regions like California in the USA and the Middle East [1]. Beyond water scarcity, these areas face a growing need for unforeseen levels of cooling, heating, and electricity, driving the demand for new sources of freshwater, such as desalinated seawater. This demand marks a shift away from traditional standalone engineering solutions towards integrated cogeneration systems. These systems, which produce both freshwater and energy, are increasingly sought after, especially when powered by renewable energy sources to reduce greenhouse gas emissions [2]. Consequently, the integration and optimization of these systems with renewable energies, focusing on efficient configurations and advanced heat recovery methods, have become critical areas of interest within the research community.

Optimizing the techno-economic performance of cogeneration systems through the recovery of waste heat is a pivotal element of various applications. In one such example

of this optimization, leveraging the recovery of waste heat in the natural gas cycle within a power and freshwater cogeneration configuration proved to significantly reduce total annual costs to USD 1,559,491, yielding an annual return on investment of USD 598,833 [3]. Dos Reis et al. [4] developed a new methodology for heat, power, and cooling cogeneration by recovering waste heat from bottoming cycles; they achieved 26.15% energy efficiency with a 6.085% saving on primary energy. Integrated recovery of waste heat, carbon capture, and dehumidification could improve the power generation and thermal efficiency of a coal-fired power plant by 13.34% and 5.74%, respectively, within 5.36 years compared with recovering capex [5]. Moreover, waste heat recovered from a pressurized water reactor has shown the potential to elevate the economic efficiency of direct-contact membrane distillation, allowing this method to compete with traditional multi-effect distillation (MED) and multi-stage flash (MSF) desalination technologies [6]. This achievement is particularly noteworthy, given that the standalone MSF process traditionally exhibits the smallest water loss among freshwater production methods [7]. Esmaeilion et al. showed that exergetic performance of integrated systems provides limited opportunities for optimization [8]. Thus, environmental considerations play a crucial role in the configuration of components, performance enhancement, and system optimization [9]. Considering the drop in the performance of gas turbines (GTs) in hot seasons, studies like those by Abdulrahim and Chung [10] have compared the efficacy of evaporative cooling and solar energy-fired absorption refrigeration systems in improving the performance of said cogeneration systems. Their results showed that the given plant's overall exergy efficiency could increase by 5.96 to 6.73% after reducing the compressor inlet air temperature. Other research has investigated the use of evaporative coolers, spray inlet coolers, fogging systems, and mechanical vapor compression for similar purposes [11]. However, the potential of utilizing cooling from combined desalination and refrigeration systems to chill the air taken in by GT compressors in integrated systems remains an underexplored topic.

Ensuring the sustainability of energy systems necessitates a comprehensive approach that extends beyond energy efficiency to include the minimization of heat rejection and emissions. The circular integration of thermal and chemical processes presents a promising avenue for producing freshwater, meeting other needs without resorting to hazardous emissions or significant water losses for the purpose of cooling [12]. Although strides have been made in mitigating climate change through such approaches, the achievement of net-zero carbon emissions cannot only be the responsibility of biogas-driven facilities. Renewable forms of energy and hydrogen units are two promising alternative options for the reliable operation of eco-friendly community systems [13]. An integrated binary geothermal energy system, as a green energy-based example, could ensure a capacity of 0.019 kg/s of green methanol with 36.96% energy and 39.31% exergy efficiencies through the elaborate production and use of hydrogen [14]. Despite the hybridization approach being more economic, long-term hydrogen storage and conversion are attracting great attention due to the greater exergy efficiency they can provide. For instance, Rodríguez et al. [15] reached a 52.04% exergy efficiency by integrating a sulfur–iodine thermochemical cycle and an MSF desalination process in a hydrogen and freshwater cogeneration system. Contrarily, Al-Fadhli et al. [16] minimized total annual costs by retrofitting desalination facilities, thermal power plants, and battery storage with photovoltaic arrays. They showed that maintaining a consistent capacity in a photovoltaic array is feasible with carbon tax rates ranging from USD 20 to 120/t CO_2. As carbon prices rise and corporations commit more strongly to decarbonization, the need for efficient, long-term planning in order to navigate the complex landscape of cogeneration technologies becomes more imminent [17]. Optimization models will therefore have a critical role in guiding the more sustainable development of energy systems.

Optimization techniques have been extensively applied in order to enhance the design and operation of model-based cogeneration systems. Mosaffa et al. [18] applied parametric optimization to a parallel combined cooling and power cogeneration system and reduced the payback period to 4.8 years by reaching energy and exergy efficiencies of 68.8% and 37%.

Sun et al. [19] demonstrated how a multi-objective optimization model could harmonize the thermodynamic and economic aspects of a cooling and power cogeneration system, managing to decrease the economic costs and exergy destruction rate by 1.6% and 31.5%, respectively. Such models have also been beneficial for cogeneration systems involving freshwater production and cooling/heating, which typically utilize either membrane-based methods like reverse osmosis or thermal techniques such as MSF and MED [20]. These desalination processes, requiring both power and heat, are often paired with vapor compression or absorption refrigeration systems to leverage common energy sources (such as the heat that is rejected from gas turbine plants), thus enhancing system efficiency. One such optimal electricity and freshwater cogeneration system reached 45.6% exergy efficiency, a 2.716 USD/GJ total product cost rate, and 30.26 kg/s CO_2 emission using natural gas and a heliostat solar field [21]. Using a multi-objective particle swarm optimization algorithm, the exergy efficiency, net output power, and net present value of a power and heating cogeneration system increased to 44.083%, 8008.6 kW, and USD 14.566 M, respectively [22]. Although a classical linear programming technique for multidimensional analysis of preference may increase the net power and freshwater production rate of a cogeneration system from 5601 kW and 39.5% at the base configuration to 7070.52 kW and 41.16% after optimization [23], advanced metaheuristic optimization tools are usually chosen to improve both the energy and exergy efficiency of power–freshwater cogeneration systems. Using a genetic algorithm, Jafarzad et al. [24] improved the energy and exergy efficiency of a power–freshwater cogeneration system by 2.18 and 1.54 times, respectively. Charmchi et al. [25] extended the model to a many-objective optimization formulation and proposed a flexible system that can operate in various modes. Despite these advancements, potential green energy supply systems remain underexplored.

Acknowledging the indispensability of renewable forms of energy as cogeneration systems adapt to the conditions of climate change and transition to a net-zero future, this study introduces a novel approach for designing an efficient, renewable-energy-driven integrated cooling–freshwater system. In accordance with the aforementioned research gaps, we present three innovations.

1. To investigate the potential of cooling the inflow air of a GT to enhance overall thermodynamic performance, a novel configuration of the integrated system uses an internal heat exchanger to transfer heat to a bottoming refrigeration cycle.
2. In response to the lack of a general computational platform that links iterative thermal simulation models with vectorized mathematical models of renewable energies, a new integrated thermo-environ-economic framework is proposed for comprehensive system evaluation.
3. The variable of modified total annual cost (MTAC) is introduced as a novel economic target to reduce the computational costs of the large optimization models.

The rest of the paper consists of three major parts. Firstly, thermodynamic, economic, exergoeconomic, and environmental models of the integrated system are developed to form an optimization platform. Secondly, a model-based integrated renewable-energy-driven cogeneration system is validated using a case study from the Middle East. Finally, the results are discussed—considering the uncertainties of fossil fuel prices, solar radiation, and wind speed—via a sensitivity analysis conducted under optimum conditions.

2. Materials and Methods

This section details the configuration, modeling framework, and optimization strategy of the proposed system. Section 2.1 elucidates the layout of the proposed system, which integrates three interdependent subsystems into a single cogeneration system with internal heat recovery potential. Subsequently, the system is mathematically modeled using basic thermodynamic principles (Section 2.2) and incorporates primary economic, exergoeconomic, and environmental analyses within a new modeling platform (Section 2.3). An iterative mathematical model simulates the thermal units, while vectorized programming techniques are used to model the green units. These three analyses are essential for

evaluating the system's performance. The variables derived from these primary analyses form the terms of a novel optimization objective function discussed in Section 2.4. This objective function determines the system's final configuration and the energy trade among the subsystems. Finally, the sensitivity of the optimal system to various renewable and non-renewable fuels is analyzed in Section 2.5, assessing the robustness of the model-based system with respect to different fuel inputs.

2.1. System Configuration

As depicted in Figure 1, the proposed integrated system comprises three principal subsystems: the integrated MED, absorption heat pump (ABHP), and vapor compression refrigeration (VCR) subsystem, collectively referred to as the MAV subsystem within this study. Additionally, it includes a combined heat and power (CHP) subsystem, and a hybrid renewable power (HRP) subsystem equipped with battery and hydrogen storage options, denoted HRP/BH. The MAV subsystem, presented in a blue polygon in Figure 1, is responsible for generating the integrated system's freshwater and cooling outputs, with its requisite heat and power supplied by the CHP and HRP/BH subsystems. A portion of the cooling produced by the VCR unit is utilized to cool the air in the CHP unit's compressor inlet, thereby boosting efficiency. Freshwater generated in the MAV subsystem's final stage undergoes expansion via the expansion valve (EV_2), enabling it to flow through the evaporator. In the evaporator, the saturated liquid turns to saturated vapor by absorbing heat from the surrounding air. The vapor refrigerant, saturated upon exiting the evaporator, is split into two pathways: one is directed to the absorber after compression by the low-pressure compressor, while the other is compressed by a high-pressure compressor and channeled to the MED unit's first stage to meet its energy requirements. The high-pressure compressor functions as a mechanical heat pump for the MED unit, relying on electricity instead of a hot source. The refrigerant compressed by the low-pressure compressor is absorbed by the concentrated solution in the absorber before being pumped through a solution heat exchanger (SHX) to the generator at elevated pressure. The MED subsystem's heating steam is sourced from two streams: the first is produced by the LiBr-H_2O boiling off due to heat from the heat recovery steam generator (HRSG) in the generator; the second stream results from a part of the vapor condensed in the MED-ABHP unit's first stage, which is vaporized by reclaiming heat from both the solution and the compressed vapor in the absorber.

As shown in Figure 1, the hot steam is introduced to the tube side within the first stage of the MED-ABHP unit, before being condensed by releasing its latent heat into the feed water for evaporation. Some of the resulting condensate recirculates to the absorber, while the rest enters the first flashing box. Demisted vapor formed in the first stage and the flashed vapor from the first flashing box are used together as heating sources in the first pre-heater to preheat the feed water to the first stage. This combined vapor then moves to the second stage, acting as the heat source for vaporizing the feed water therein. This cycle repeats across all stages, culminating with the vapor from the final stage passing through a condenser. Part of this condensed vapor functions as a refrigerant (via EV_2), with the remainder being directed to the distillate tank as resulting freshwater. The cooling water for the MED unit is split; one stream is used as feed water across stages, and the other is discharged back into the sea. The electricity needed for the high- and low-pressure compressors and the solution pump is provided by the CHP and HRP/BH subsystems, and the heat needed in the generator is provided by the HRSG of the CHP subsystem. In the CHP subsystem, air cooled by the MAV system's evaporator is compressed by an air compressor (AC) and then fed into a combustion chamber (CC) where fuel is added. The resulting hot gas expands through a gas turbine (GT), generating shaft work to power both the AC and a generator (G). This expanded gas is then processed through an HRSG component, which recovers the waste heat from the exhaust gas to generate motive steam for the MAV generator. The CHP subsystem, restricted by purple lines in Figure 1, operates on purified natural gas.

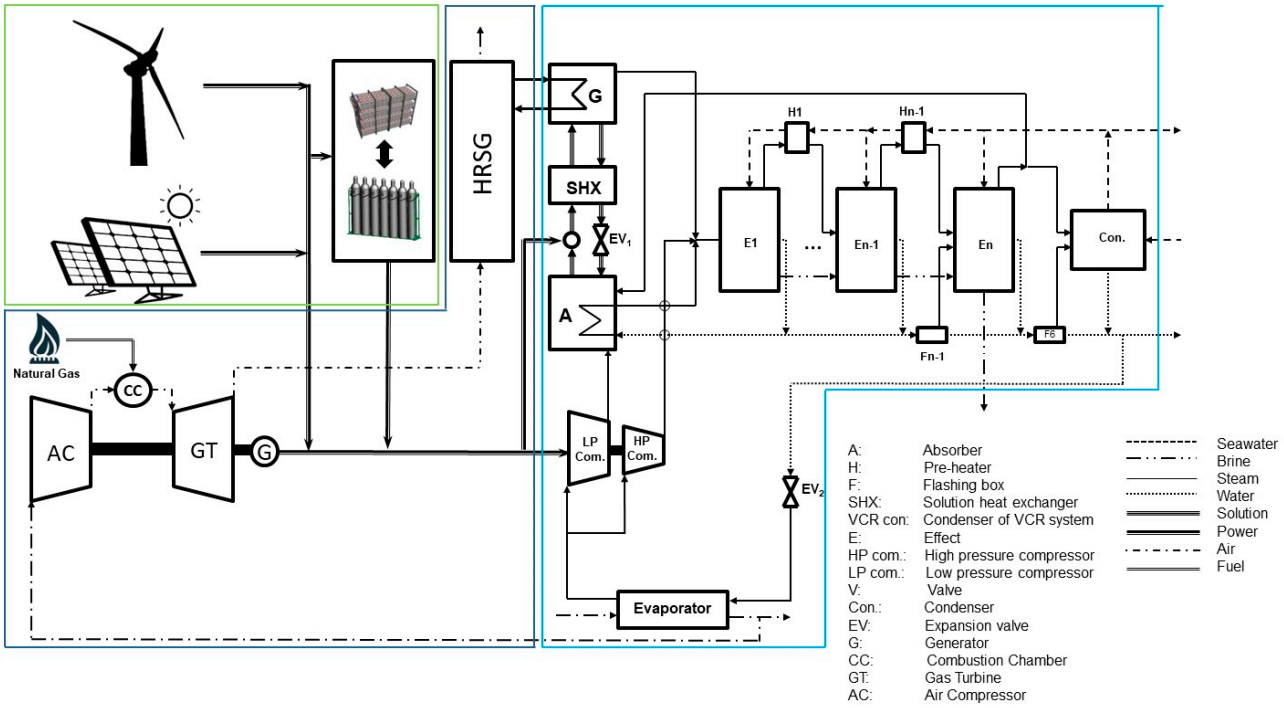


Figure 1. Schematic representation of the proposed integrated system.

In the HRP/BH subsystem, as represented by a green rectangle in Figure 1, electricity from a wind turbine is utilized to power the compressors and pump directly. Any surplus electricity from the wind turbine undergoes conversion to direct current (DC) via a rectifier. This DC power, along with that generated by solar photovoltaic (PV) panels, is initially used to charge the battery system. Once the battery reaches full capacity, additional electricity is routed to a DC/DC converter, enhancing system efficiency through voltage stabilization. This stable electrical output is then used in a deionizer for water deionization, the product of which is supplied to an electrolyzer. The electrolyzer's function is to split water into hydrogen and oxygen, which are subsequently stored in separate tanks for later use. The electrolyzers and hydrogen facilities are shown in schematic figures in the box at the right-hand side of the solar PVs and wind turbined in Figure 1. Should the electricity generated by the wind turbine fall short of the system's demands, the stored DC power is mobilized by discharging the battery, converting it to alternating current (AC) using an inverter. If the battery is fully depleted, the system then taps into the stored hydrogen and oxygen, channeling them into a fuel cell to generate electricity, with water produced as a by-product. The electricity from the fuel cell, adjusted for voltage compatibility with the DC bus via a DC/DC converter, supplements the system's power supply. The hierarchical nature of this electricity management strategy, prioritizing battery discharge before fuel cell utilization, guides the optimization of the integrated system's design.

2.2. Mathematical Model

Figure 2 shows the computational framework of the proposed model, which integrates thermodynamic, environmental, and economic models for each subsystem to calculate overall exergy destruction, total annual costs (TACs), and hazardous emissions. As indicated in the figure, the rate of cooling and freshwater production is influenced by the refrigerant ratio within the MAV subsystem. The power demand dictates the sizing of the CHP and HRP/BH subsystems based on the power ratio (PR). The red arrows show the critical variables calculated while simulating a subsystem and used in modeling other subsystems. Following the management strategy outlined in Section 2.1, the models for all subsystems are defined, facilitating the calculation of the exergy destruction costs, MTAC, and emissions of CO and NOx for the entire integrated system. These variables then

serve as inputs for an optimization platform. Detailed mathematical models for all three subsections are provided in subsequent sections to elucidate the proposed methodology.

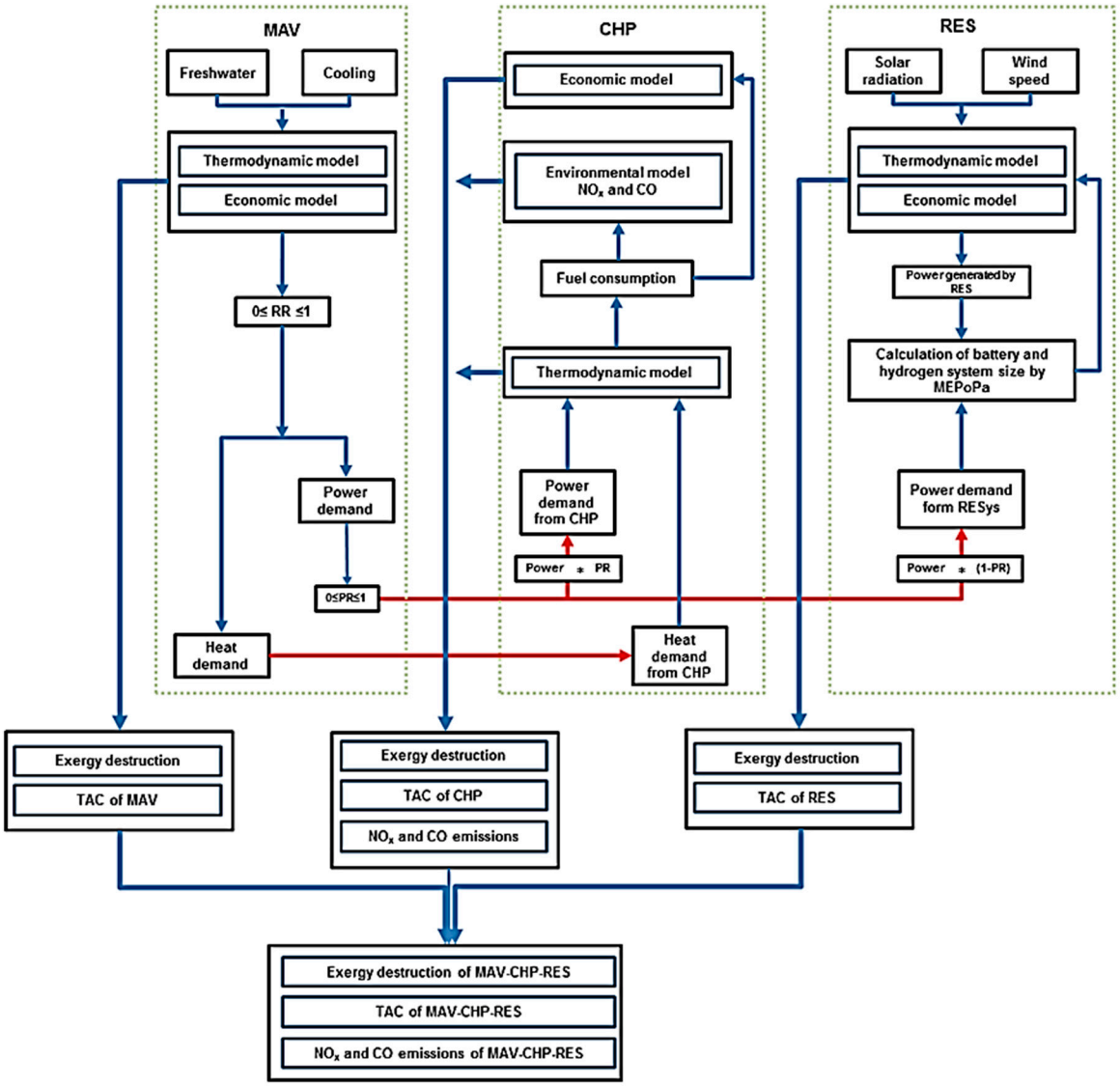


Figure 2. Thermo-environ-economic modeling framework.

Several simplifying assumptions were made in the development of the thermodynamic model of the system, as outlined below [26]:

- The system operates under steady-state conditions.
- Heat losses and pressure drops in piping and components are considered negligible.
- The concentration of water/lithium bromide (LiBr) in the steam phase is assumed to be zero.
- The water/LiBr solution at the generator and absorber outlets is in a saturated state.
- The refrigerant at the outlets of the evaporator and condenser in the VCR cycle is saturated.
- All gases are treated as ideal gases.

2.2.1. The MAV Subsystem

The MAV components are simulated according to the modeling assumptions and the mathematical equations in this section. The mass, concentration, and energy bal-

ance of the generator, absorber, evaporator, EV, and SHX components are presented in Equations (1)–(3), respectively [27,28].

$$\sum \dot{m}_{in} = \sum \dot{m}_{out} \tag{1}$$

$$\sum \dot{m}_{in} x_{in} = \sum \dot{m}_{out} x_{out} \tag{2}$$

$$\dot{Q} = \sum \dot{m}_{in} h_{in} - \sum \dot{m}_{out} h_{out} \tag{3}$$

where $\dot{m}$ is the mass flow rate, x is the solution concentration, h is the specific enthalpy, and $\dot{Q}$ is the net heat rate of the component. The subscripts *in* and *out* represent the inlet and outlet streams, respectively. The power consumption ($\dot{W}$) of the pump is given by Equation (4) [29].

$$\dot{W}_{Pu} = \frac{\sum \dot{m}_{out} h_{out} - \sum \dot{m}_{in} h_{in}}{\eta_{Pu}} \tag{4}$$

where η is the isentropic efficiency, and the subscript Pu represents the pump. The MED unit is modeled using the equations developed by Esfahani et al. [30] and Charmchi et al. [25]. Mass balance equations of the first and second to nth stages and the end condenser are given by Equations (5) through (7), respectively.

$$\dot{m}_{B_1} = \dot{m}_{F_1} - \dot{m}_{D_1} \tag{5}$$

$$\dot{m}_{B_i} = \dot{m}_{F_i} + \dot{m}_{B_{i-1}} - \dot{m}_{D_i} + \left[y_{i-1} \cdot \left(\dot{m}_{D_r} + \sum_{j=1}^{i-2} \dot{m}_{D_j} \right) \right] - \left[(i-1) \cdot \dot{m}_{F_{i-1}} \cdot y_{i-1} \right] \tag{6}$$

$$\dot{m}_{D_{Con.}} = \dot{m}_{D_n} - \dot{m}_{D_r} + \left[y_n \cdot \left(\dot{m}_{D_r} \cdot \sum_{i=1}^{n-1} \dot{m}_{D_i} \right) \right] \tag{7}$$

where subscripts B, F, and D represent brine, feed, and distillate streams, respectively. Subscripts i, r, and *Con.* represent the number of stages, entrained steam, and condenser, respectively, and y is the flash ratio. The produced freshwater mass flow rate ($\dot{m}_{\mathrm{Pr}}$) is given by Equation (8).

$$\begin{aligned} \dot{m}_{\mathrm{Pr}} = & \left[(1 - y_n) \cdot \left(\dot{m}_{D_r} + \sum_{i=1}^{n-1} \dot{m}_{D_i} \right) \right] - \left[y_{n-1} \left(\dot{m}_{D_r} + \sum_{i=1}^{n-2} \dot{m}_{D_i} \right) \right] \\ & - \left[y_{n-3} \left(\dot{m}_{D_r} + \sum_{i=1}^{n-4} \dot{m}_{D_i} \right) \right] - \left[y_{n-4} \left(\dot{m}_{D_r} + \sum_{i=1}^{n-5} \dot{m}_{D_i} \right) \right] - \left(y_{n-5} \cdot \dot{m}_{D_r} \right) + \dot{m}_{D_{Con.}} - \dot{m}_{ref} \end{aligned} \tag{8}$$

where $\dot{m}_{ref}$ is the refrigerant mass flow rate. The salinity balance equations of the first, and second to nth stages are given in Equations (9) and (10), respectively.

$$X_{sw} \cdot \dot{m}_{F_1} = X_{B_1} \cdot \dot{m}_{B_1} \tag{9}$$

$$X_{sw} \cdot \dot{m}_F + X_{B_{i-1}} \cdot \dot{m}_{B_{i-1}} = X_{B_i} \cdot \dot{m}_{B_i} \tag{10}$$

where X is salinity, and subscripts i and sw represent the number of stages and seawater, respectively.

Energy balance equations of the first stage and second to nth stages are given by Equations (11) and (12), respectively.

$$\dot{m}_{D_1} \cdot L_1 + \left(\dot{m}_{F_1} \cdot \left[(C_p(T_1) \cdot T_1) - \left(C_p\left(T_{f_1}\right) \cdot T \right)_1 \right] \right) = \dot{m}_0 \cdot L_0 \tag{11}$$

$$\begin{aligned} & \dot{m}_{D_i} \cdot L_i + \left[\dot{m}_F \cdot C_p \left(T_i - T_{f_i} \right) \right] = \left(\dot{m}_{D_{i-1}} \cdot L_{i-1} \right) \\ & + \left[y_{i-1} \cdot \left(\dot{m}_{D_r} + \sum_{j=1}^{i-2} \dot{m}_{D_j} \right) \cdot L_{i-1} \right] - \left[(i-1) \cdot \dot{m}_{F_{i-1}} \cdot y_{i-1} \cdot L_{i-1} \right] + \left[\dot{m}_{B_{i-1}} \cdot C \cdot (\Delta T_{i-1,i}) \right] \end{aligned} \tag{12}$$

where L is the latent heat of the stream. $\dot{m}_0$ is the mass flow rate of the motive steam, and $\Delta T_{i-1,i}$ is temperature difference between the ith and $(I-1)$th effects, which is assumed to be equal among the effects to achieve the optimum operating conditions, as outlined in Equation (13).

$$\Delta T_{i-1,i} = T_{i-1} - T_i = \Delta T_{MED} \tag{13}$$

The power consumptions of the low- and high-pressure compressors ($\dot{W}_{com}$) are obtained using Equation (14).

$$\dot{W}_{com} = \dot{m}_{com} \cdot (Cp_{out} \cdot T_{out} - Cp_{in} \cdot T_{in}) \tag{14}$$

where subscript *com* represents the compressors, Cp is the specific heat capacity at constant pressure, and T is the temperature, obtained using Equation (15) [12].

$$T_{out} = T_{in} \times \left(1 + \frac{1}{\eta_{com}} \left(r_{com}^{\frac{\gamma_{steam}-1}{\gamma_{steam}}} - 1\right)\right) \tag{15}$$

where η_{com} is the isentropic efficiency of the compressor, γ_{steam} is the heat ratio of steam, and r_{com} is the pressure ratio of the compressor, calculated using Equation (16).

$$r_{com} = \frac{P_{out}}{P_{in}} \tag{16}$$

where P is the pressure. The refrigerant ratio from the low-pressure compressor to the high-pressure compressor (RR) is calculated by Equation (17).

$$\mathrm{RR} = \frac{\dot{m}_{\mathrm{HP},com}}{\dot{m}_{\mathrm{HP},com} + \dot{m}_{\mathrm{LP},com}} \tag{17}$$

where the subscripts HP and LP denote the high-pressure and low-pressure compressors, respectively. The ratio, RR, indicates the distribution of refrigerant flow between the low-pressure and high-pressure turbines within the system, ranging from 0 to 1. As depicted in Figure 2, RR plays a pivotal role in defining the configuration of the adaptable MAV subsystem. With an RR value of 0, all refrigerant from the evaporator is directed to the low-pressure compressor, thereby increasing the MAV subsystem's heat demand. Conversely, with the RR set to 1, the entire refrigerant flow from the evaporator is compressed by the high-pressure compressor, leading to a reduction in the MAV subsystem's heat requirement. Table 1 outlines the initial operating and thermodynamic parameters for the MAV subsystem [25,30].

Table 1. Initial operating conditions and thermodynamic parameters of the MAV subsystem.

Variable	Quantity	Unit
Effect number	6	-
$P_{motive\ steam}$	500	kPa
η_{com}	91	%
η_{pump}	91	%
X_{sw}	30,000	ppm
X_{B6}	70,000	ppm
$T_{evaporator}$	6	°C
$Q_{freshwater}$	15,000	m^3/d
$Q_{cooling}$	30,000	kW

2.2.2. The CHP Subsystem

The thermodynamic models developed by Ifaei et al. [12] were adopted to simulate the CHP subsystem. Equations (14) to (16) are used to determine the power consumption

and thermodynamic properties of the airflow exiting the AC. The mass and energy balance equations of the combustion chamber (CC) are given in Equations (18) and (19).

$$\dot{m}_{flue} = \dot{m}_{air} + \dot{m}_{fuel} \tag{18}$$

$$\begin{aligned} &\dot{m}_{air}h_{air} + \dot{m}_{fuel}LHV_{fuel} + \dot{m}_{water}h_{water} = \dot{m}_{flue}h_{flue} \\ &+(1-\eta_{CC})\dot{m}_{fuel}LHV_{fuel} + \dot{m}_{steam}h_{steam} \end{aligned} \tag{19}$$

where the subscript *flue* represents the outlet flue gas, LHV is the lower heating value, and η_{CC} is the efficiency of the combustion chamber.

The power generated by the gas turbine ($\dot{W}_{GT}$) and the net power generated in the CHP ($\dot{W}_{net}$) are obtained using Equation (20)

$$\dot{W}_{GT} = \left(\dot{m}_{water} + \dot{m}_{flue}\right) Cp_{inlet}(\Delta T_{GT}) \tag{20}$$

$$\dot{W}_{net} = \dot{W}_{GT} - \dot{W}_{AC} \tag{21}$$

where Cp_{inlet} is the heat capacity of the GT inflow, ΔT_{GT} is the temperature difference between GT's inlet and outlet streams, and $\dot{W}_{AC}$ is the power consumed by the air compressor. The detailed computational approach for the combustion model, along with all necessary constants, is outlined in [12]. Key constants employed in this analysis are consolidated in Table 2.

Table 2. Initial operating conditions and thermodynamic parameters of the CHP subsystem.

Parameter	Value	Unit
η_{com}	91	%
η_{GT}	91	%
η_{cc}	91	%
$P_{Steam\text{-}HRSG}$	500	kPa
Fuel	Methane	---
LHV_{fuel}	51,400	kJ/kg
Compressor inlet air temperature	25	°C
Compressor inlet air pressure	1	bar
HRSG outlet gas temperature	140	°C
AFR	10.42	-

2.2.3. The HRP/BH Subsystem

The HRP/BH subsystem incorporates solar PVs, wind turbines, electrolyzers, fuel cells, and hydrogen storage tanks. The power output of the solar PVs was obtained using Equation (22) [31].

$$P_{PV} = Y_{PV} f_{PV} \left(\frac{G_T}{G_{T,STC}}\right)[1 + \alpha_P(T_c - T_{c,STC})] \tag{22}$$

where Y_{PV} is the power output of PV module under standard test conditions (STC), f_{PV} is the PV's derating factor, α_P is the temperature coefficient of power, T_c is PV cell's temperature, $T_{c,STC}$ is the PV cell's temperature under STC, and G_T is the total solar radiation on the tilted PV module, which is determined using Equation (23).

$$G_T = G_{DB} + G_{DC} + G_R \tag{23}$$

where G_B, G_D, and G_R represent the direct beam, diffuse component, and ground-reflected component of solar radiation, respectively.

T_c is obtained using Equation (24).

$$T_c = \frac{T_a + (T_{c,NOCT} - T_{a,NOCT})\left(\frac{G_T}{G_{T,NOCT}}\right)\left(1 - \frac{\eta_{mp,STC}\left(1-\alpha_p T_{c,SCT}\right)}{\tau\alpha}\right)}{1 + (T_{c,NOCT} - T_{a,NOCT})\left(\frac{G_T}{G_{T,NOCT}}\right)\left(\frac{\alpha_p \eta_{mp,SCT}}{\tau\alpha}\right)} \quad (24)$$

where T_a is the ambient temperature, $T_{c,NOCT}$ is the nominal operating cell temperature, $T_{a,NOCT}$ is the ambient temperature at which the NOCT is defined (20 °C), $G_{T,NOCT}$ is the solar radiation at which the NOCT is defined (0.8 kW/m^2), $\eta_{mp,STC}$ is the maximum power point efficiency under STC, τ is the solar transmittance of any cover over the PV array, and α is the solar absorptance of the PV array. Table 3 details the characteristics of the PV module utilized in this study, with additional modeling information available in [31].

Table 3. Technical data of the solar PV panel.

Parameter	Value	Unit
Rated capacity	250	W
Derating factor	90	%
Nominal operating cell temperature	46	°C
Temperature coefficient	−0.45	%/°C
Efficiency at standard test condition	15.36	%
lifetime	25	years
Dimensions	1.64 × 0.992	m

The power output of the wind turbines (P_{WT}) is obtained using Equation (25).

$$P_{WT} = 0.5(1 - F)\rho_{hub} V_{hub}^3 A C_{WT} \quad (25)$$

where F is the loss factor, ρ_{hub} is the air density at the hub height, V_{hub} is the air speed at the hub height, A is the swept area by the turbine's blades, and C_{WT} is maximum theoretical efficiency of the turbine. The characteristics of the wind turbine used in this study are presented in Table 4, and the further modeling details can be found in [31].

Table 4. Technical data of the wind turbine.

Parameter	Value	Unit
Rated power	100	kW
Rotor diameter	21	m
Number of rotor blades	3	-
Cut-in wind speed	2.5	m/s
Cut-out wind speed	25	m/s
Rated wind speed	12	m/s
Lifetime	15	years

The actual industrial sizes of the hydrogen storage system components, including the electrolyzer, hydrogen tank, and fuel cell, are calculated by considering the power losses based on the actual appropriate hydrogen tank electricity capacity ($AHTC_a$) and the components' efficiencies. The actual volume of the hydrogen tank ($V_{HT,a}$) is calculated using Equation (26).

$$V_{HT,a} = \frac{AHTC_a \cdot M_{HT}}{0.0658 \cdot 0.0446 \cdot H_{PT}} \quad (26)$$

where M_{HT} and H_{PT} are considered to be 2.5 m^3 and 200 bar, respectively [32].

The number of electrolyzer cells ($N_{EL,a}$) is obtained using Equation (27).

$$N_{EL,a} = \frac{1000 AHTC_a}{I_{EL} V_{EL} t_{AHTC_a} \eta_{EL}} \quad (27)$$

where I_{EL} is the current through the electrolyzer (A), V_{EL} is the working voltage (V), t_{AHSSC} is the time interval duration related to $AHTC_a$, and η_{EL} is the efficiency of the electrolyzer. I_{EL}, and V_{EL} are considered to be 3.8 A and 11.32 V, respectively [12].

The number of cells in the proton exchange membrane fuel cell (PEMFC) can be obtained using Equation (28).

$$N_{FC,a} = \frac{1000 AHTC_a}{\eta_{FC} I_{FC} V_{FC} t_{AHTC}} \tag{28}$$

where N_{FC} is the number of fuel cells and I_{FC} and V_{FC} are the output current and voltage of the fuel cell, which are considered to be 2.92 A and 4.93 V [12]. t_{AHTC} is the time interval duration associated with $AHTCa$, and η_{FC} is the efficiency of the fuel cell. The technical properties of the energy storage system used in this study are summarized in Table 5 [12,33,34].

Table 5. Technical data of energy storage facilities.

Parameter	Value	Unit
Battery		
Efficiency	90	%
Lifetime	4	years
Operating and maintenance cot (% of capital cost)	1	%
Fuel cell		
Efficiency	50	%
Lifetime	40,000	hours
I_{FC}	2.92	A
V_{FC}	4.93	V
Electrolyzer		
Efficiency	75	%
Lifetime	25	years
I_{EL}	3.8	A
V_{EL}	11.32	V
Hydrogen tank		
Efficiency	95	%
Lifetime	25	years
M_{HT}	2.5	m^3
H_{PT}	200	bar
Convertor		
Efficiency	95	%
Lifetime	16	years
Compressor		
Efficiency	70	%
Lifetime	10	years

2.3. System's Analyses

To integrate the fundamental mathematical model with an optimization framework, it is essential to conduct economic, exergoeconomic, and environmental analyses. These analyses serve as a computational bridge, facilitating the transition from initial conceptual models to optimized configurations.

2.3.1. Economic Analysis

The economic performance of the system was analyzed using the models developed by Ifaei et al. [12] and Charmchi et al. [25] to obtain *TAC* as given in Equation (29).

$$TAC = TCC \frac{ir(1+ir)^{lt}}{(1+ir)^{lt}-1} + AOC \tag{29}$$

where TCC is the total capital cost, ir is the interest rate, lt is the lifetime of the project, and AOC is the annual operation costs obtained using the data in Table 6. The TCC is computed using Equation (30).

$$TCC = \sum PEC_i + C_{con} \quad (30)$$

where PEC_i is the purchased equipment costs, and C_{con} represents the contingency costs that include civil and construction, engineering and supervision costs, which is assumed to be 0.15 of the total purchased costs at the computation year, 2023 [12].

Table 6. Major economic constants and parameters.

Parameter	Value	Unit	Ref.
Battery			
Capital cost	120	$/kWh	[35]
Fuel cell			
Capital cost	3000	$/kW	
Replacement cost	2500	$/kW	[33]
Operating and maintenance cost	0.02	$/h	
Electrolyzer			
Capital cost	2000	$/kW	[33]
Replacement cost	1500	$/kW	[33]
Operating and maintenance cost	20	$/year	[33]
Hydrogen tank			
Capital cost	1300	$/kg	[33]
Replacement cost	1200	$/kg	[33]
Operating and maintenance cost	15	$/year	[33]
Converter			
Capital cost of	800	$/kW	[33]
Replacement cost	750	$/kW	[33]
Operating and maintenance cost of converters	6.5	$/year	
Compressor			
Capital cost	2500	$/kW	[25]
Operating and maintenance cost (% of capital cost)	0.5	%	[25]
Wind turbine			
Capital cost	150,000	$/unit	[35]
Replacement cost	130,000	$/unit	[35]
Operating and maintenance cost	2500	$/year	[35]
Solar PV			
Capital cost	350	$/module	[35]
Replacement cost	350	$/module	[35]
Operating and maintenance cost	25	$/kW/year	
CHP			
Fuel price	10.1	$/MWh	[12]
Absorber			
Reference capital cost	16,500	$	[12]
Overall heat transfer coefficient	0.7	kW/m^{2}K	[25]
MAV generator			
Reference capital cost	17,500	$	[12]
Overall heat transfer coefficient	1.5	kW/m^{2}K	[25]
SHX			
Reference capital cost	12,000	$	[12]
Overall heat transfer coefficient	1	kW/m^{2}K	[25]

PEC of the electro-mechanical components is obtained by the nonlinear equations from [12,25,31], and that of the heat-exchanging units (PEC_{HX}), such as the absorber, evaporator, and SHX are obtained using Equation (31).

$$PEC_{HX} = C_i\left(\frac{Q_i}{U_i \Delta T_{lm,i} A_{i,ref}}\right)^{0.6} \quad (31)$$

where C_i is the cost of the ith component in the reference year, Q_i is the transferred heat rate, U_i is the overall heat transfer coefficient, $A_{i,ref}$ is the area of the ith reference component, and $\Delta T_{lm,i}$ is the logarithmic mean temperature difference. The economic constants and parameters are summarized in Table 6. Some parameters are directly obtained from cited references [12,25,35], whereas others are harmonized to be used in this model.

2.3.2. Exergoeconomic Analysis

The exergy destruction rate ($\dot{E}x_{De}$) of each component was obtained using the exergy models developed by Charmchi et al. [25]. The exergy balance equation is given in Equation (32).

$$\dot{E}x_{De} = \sum(\dot{E}x_{in} - \dot{E}x_{out}) + \sum(\dot{W}_{in} - \dot{W}_{out}) + \sum((1 - \frac{T_{DS}}{T}).\dot{Q})_{in} - \sum((1 - \frac{T_{DS}}{T}).\dot{Q})_{out} \quad (32)$$

where $\dot{E}x$, $\dot{W}$, T_a, T, and $\dot{Q}$ are the exergy rate, power, temperature of the dead state (298 K), absolute temperature, and heat rate of the stream, respectively. The exergy rate of the fuel ($\dot{E}x_F$), product ($\dot{E}x_P$), and lost ($\dot{E}x_L$) streams are obtained using Equation (33) [25].

$$\dot{E}x_{De} + \dot{E}x_L = \dot{E}x_{Fu} - \dot{E}x_{\mathrm{Pr}} \quad (33)$$

The exergoeconomic analysis was conducted using the annual cost flow of each component in a cost-flow approach [36]. The exergoeconomic balance equations of each component of the system are given in Equations (34)–(36) [25].

$$\dot{Z} = \sum \dot{C}_W + \sum \dot{C}_{out} - \sum \dot{C}_{in} - \sum \dot{C}_Q \quad (34)$$

$$\dot{C} = c_k.\dot{E}x \quad (35)$$

$$\dot{Z} = \dot{Z}_I + \dot{Z}_R \quad (36)$$

where $\dot{C}$ is a cost rate of the exergy, c is the unit cost, and $\dot{Z}$ is the cost rate of a component obtained from the economic model detailed in Section 2.3.1. The subscripts W, Q, I, and R represent the power, heat, investment and replacement, respectively.

2.3.3. Environmental Analysis

The environmental analysis encompasses hazardous emissions due to combustion of fossil fuel in the GT. Here, we calculate CO and NOx emissions as the indicators of the environmental analysis, as outlined in Equations (37) and (38).

$$\dot{m}_{NOx} = \frac{0.15E16\dot{m}_{fuel}{t_r}^{0.5}\exp(\frac{-71100}{T_{PZ}})}{P_{CC}^{0.05}(\frac{\Delta P_{CC}}{P_{CC}})^{0.5}} \quad (37)$$

$$\dot{m}_{CO} = \frac{0.179E9\dot{m}_{fuel}{t_r}^{0.5}\exp(\frac{78000}{T_{PZ}})}{P_{CC}^{2}t_r(\frac{\Delta P_{CC}}{P_{CC}})^{0.5}} \quad (38)$$

where τ is the retention time of the combustion chamber (0.002 s), P_{CC} is the chamber's inlet pressure, ΔP_{CC} is the pressure drop in the chamber (3%), and T_{PZ} is the adiabatic flame temperature of the chamber, which is calculated using Equations (39)–(41) and the parameters reported in [37].

$$T_{PZ} = A\sigma^{\alpha}\exp[\beta(\alpha + \lambda)^2]\pi^x\theta^y\psi^z \quad (39)$$

$$\sigma = \begin{cases} \varphi < 1 & then\ \varphi \\ \varphi \geq 1 & then\ \varphi - 0.7 \end{cases} \quad (40)$$

$$\begin{aligned} x &= a_1 + b_1\sigma + c_1\sigma^2 \\ y &= a_2 + b_2\sigma + c_3\sigma^2 \\ z &= a_3 + b_3\sigma + c_3\sigma^2 \end{aligned} \tag{41}$$

2.4. Optimization Model

Upon achieving converged solutions through the mathematical model, alongside exergoeconomic, economic, and environmental analyses, an iterative optimization model was developed. The major aspects of the model are detailed in this section.

2.4.1. Objective Function

Figure 3 shows the flowchart to obtain the objective function of the optimization model considering the whole integrated system. Accordingly, a modified total annual cost ($MTAC_{tot}$) is defined as a summation of the total cost of exergy destruction of the integrated system ($C_{De,tot}$), total annual cost of that (TAC_{tot}), and its environmental emission cost ($C_{E,tot}$) of the MAV-CHP-HRP/BH system, as given in Equation (42).

$$MTAC_{tot} = C_{De,tot} + TAC_{tot} + C_{E,tot} \tag{42}$$

where $C_{De,tot}$ is the summation of the exergy destruction costs of all components obtained by Equations (32) through (35), TAC is obtained using Equation (29), and $C_{E,tot}$ is determined considering the environmental damage cost due to CO and NOx emissions using Equation (43).

$$C_{E,tot} = \dot{m}_{NOx}c_{NOx} + \dot{m}_{CO}c_{CO} \tag{43}$$

where c_{NOx} and c_{CO} are unit damage costs of the NOx (6.853 \$/kgNOx) and CO (0.02086 \$/kgCO), respectively [38].

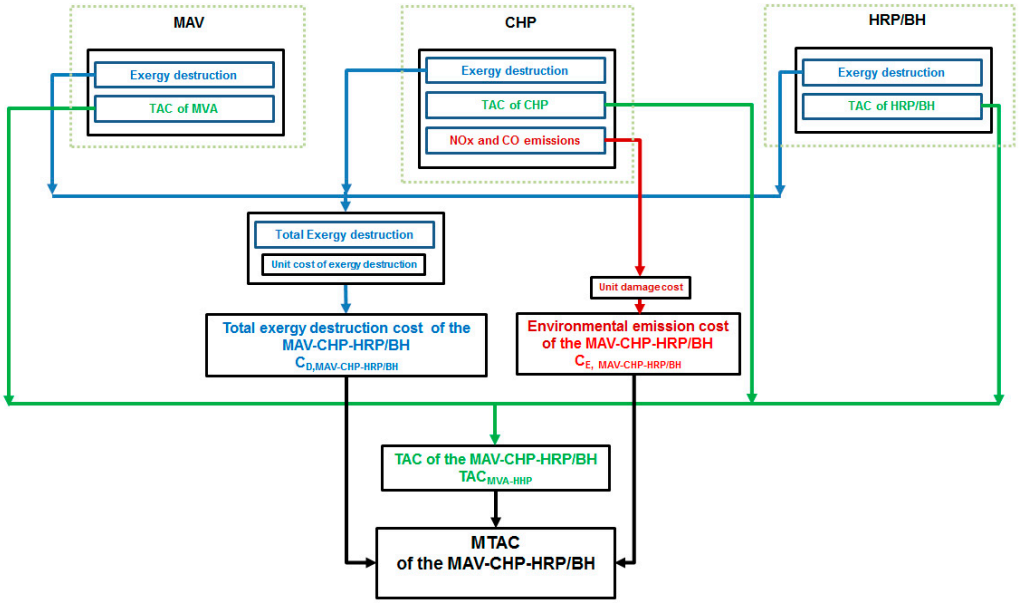


Figure 3. Computational flowchart of the objective function.

2.4.2. Decision Variables

The decision variables of the optimization model were selected based on the physical limitations of the system, logical boundaries of the feasibility space, and the design criteria for each subsystem. Within the MAV subsystem, the determination of heat and power requirements—given the demands for freshwater and cooling—relies significantly on the RR. As such, RR emerges as a crucial decision variable due to its profound impact on the integration of the MAV, CHP, and HRP/BH subsystems. In addition, the absorber pressure (P_A), temperature difference between effects of the MED system (ΔT_{MED}), temperature

of the strong solution from absorber (T_{ss}), and temperature of the weak solution from generator (T_{ws}) are selected as four key design parameters of the MVA. Their variation range is given in Table 7 [12,25]. *PR* is another crucial decision variable that substantially influences the optimization of the MAV-CHP-HRP/BH system, which plays a pivotal role in the power generation capabilities of the CHP and HRP/BH subsystems. Within the CHP subsystem, pressure ratio (*rp*), inlet and outlet temperatures of turbine ($T_{in,GT}$ and $T_{out,GT}$), and compressor inlet air temperature ($T_{in,com}$) are identified as four key physical constraints. These constraints are detailed in Table 7 [12]. For the RES subsystem, the sizes of the solar PV panels and wind turbines, along with the tilt angle of the solar PV panels, are deemed the most critical design criteria. These factors are selected as significant decision variables, impacting the system's overall efficiency and effectiveness in harnessing renewable energy [31].

Table 7. Decision variables of the optimization model.

Variable	Symbol	Unit	Range
Refrigerant ratio	RR	%	0–100
Absorber pressure	P_A	kPa	1–10
Temperature difference between MED effects	ΔT_{MED}	°C	2–7
Temperature of the strong solution from absorber	T_{SS}	°C	30–80
Temperature of the weak solution from generator	T_{WS}	°C	80–150
Power ratio	PR	%	0–100
Pressure ratio	rp	-	5–15
Fuel mass flow rate	$\dot{m}_{fuel}$	Kg/s	0–10
Inlet temperature of turbine	$T_{in,GT}$	°C	776–1200
Outlet pressure of turbine	$P_{out,GT}$	kPa	100–1000
Compressor inlet air temperature	$T_{in,com}$	°C	5–25
Number of solar PV panels	N_{PV}	Ea	0–10,000
Number of wind turbines	N_{WT}	Ea	0–10,000
Tilt angle of the solar PV panel	β_{PV}	Degree	0–80
Battery capacity	Ca_B	kWh	0–1000
Hydrogen tank capacity	Ca_H	kWh	0–1000

2.4.3. Optimization Method

The single-objective optimization problem was solved by a genetic algorithm (GA). The GA, as a parallel, heuristic, and population-based search method, was used to find the optimal solutions among a large number of feasible solutions via an evolution-based stochastic search and selection approach. The GA can solve multidimensional, non-differential, non-continues, and non-parametric problems due to its independency from error surfaces [39]. The optimum quantities of the decision variables presented in Table 7 were used to minimize the $MTAC_{tot}$ in four steps: chromosome structure and initial population size, fitness value, evolution, and terminal condition. In this study, the $MTAC_{tot}$ function, represented by Equation (42), was hired as the fitness function. The next generations were reproduced using a reproduction operator by selecting the fittest chromosomes as the patents. The crossover and mutation rates were set to be 0.5 and 0.05, respectively. The iteration was terminated by selecting the best members of the population in the feasible solution space.

2.5. Sensitivity Analysis

The sensitivity of MTAC with respect to each energy source was calculated using Equation (44) [12].

$$S_{MTAC} \cong \left.\frac{\delta f}{\delta x}\right|_{x_0} \tag{44}$$

where x represents uncertain variables (fuel price, solar radiation, and wind speed) under optimum conditions. The obtained sensitivity values are used to compare the significance of fuel price, solar radiation, and wind speed on the MTAC of the integrated system under optimum conditions.

3. Case Study

The developed model depends on spatial variables, such as the wind speed, solar radiation, and temperature. Moreover, the costs and values associated with the products of the cogeneration system can differ across various case studies. To ensure the applicability of our model, we have selected an appropriate case study for validation, details of which are discussed in this section.

3.1. Background

Kish Island, covering an area of approximately 91.5 km^2, is situated in the Persian Gulf at coordinates of 26.32° N (latitude) and 53.58° E (longitude), as depicted in Figure 4. Renowned for having the longest duration of sunshine in the region (around 3000 h annually), Kish Island ranks as the fourth most popular tourist destination in Southwest Asia, following Dubai, the UAE, and Sharm el-Sheikh [40]. It is a popular tourist attraction that receives about 1 million tourists every year [41]. Characterized by a very dry, semi-equatorial climate, Kish Island has recorded an annual average temperature of 26.6 °C and average rainfall of 180 mm over the past eight years [40]. These climatic conditions underscore the island's significant potential as a location for the deployment of desalination and refrigeration systems. Although the island's wind and bioenergy facilities have faced serious operational challenges, hybridization of these technologies with solar energy and fossil fuels could be an effective method of harnessing these green energies. This study considers the specific needs of Kish Island's western region, which requires 15,000 m^3/day of freshwater and a refrigeration capacity of 30,000 kW. Accordingly, these figures—15,000 m^3/day for freshwater production and 30,000 kW for cooling—are set as the target outputs for the integrated MAV-CHP-HRP/BH system being analyzed. In this case study, some of the technical and economic parameters of the facilities, such as electrolyzers and fuel cells, were unavailable; where necessary, these were obtained from the literature.



Figure 4. Geographical location of Kish Island.

3.2. Solar Radiation

Solar radiation data for Kish Island was sourced from the National Aeronautics and Space Administration (NASA) database [42]. Utilizing HOMER Pro Version 3.15.3 software, the 22-year average monthly solar radiation is depicted in Figure 5. This figure distinguishes between the clearness index, displayed on the right axis, and the global horizontal daily radiation (in kWh/m^2.d), shown on the left axis. According to Figure 5, solar radiation on Kish Island varies between 3.77 kWh/m^2.d and 7.99 kWh/m^2.d, with an estimated annual average of 6.103 kWh/m^2.d. Moreover, the figure indicates that higher solar radiation

levels are typically expected from March to September, whereas reduced solar radiation is more common from October to February.

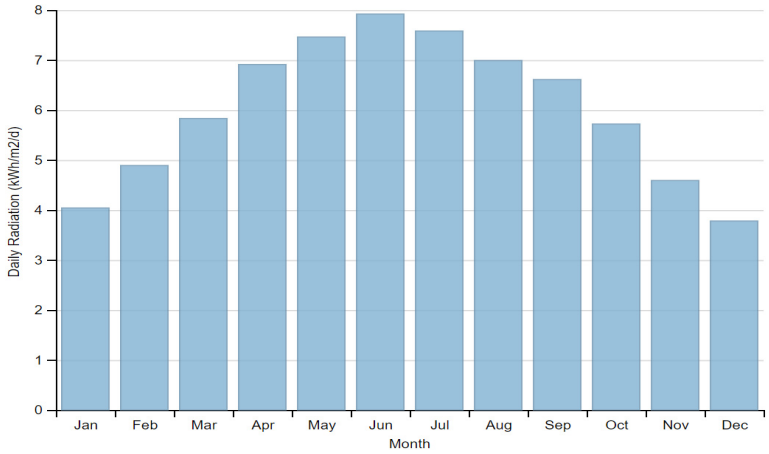


Figure 5. The average monthly solar radiation in Kish Island.

3.3. Wind Speed

Wind speed data for Kish Island was sourced from the Iran Meteorological Organization (IrMO) database [31]. The 25-year average monthly wind speed, recorded at a height of 10 m above the earth's surface in 3-h intervals, is illustrated in Figure 6. This data reveals that wind speeds on Kish Island can vary from 3.5 m/s to 6.5 m/s, with an estimated annual average wind speed of 5.03 m/s.

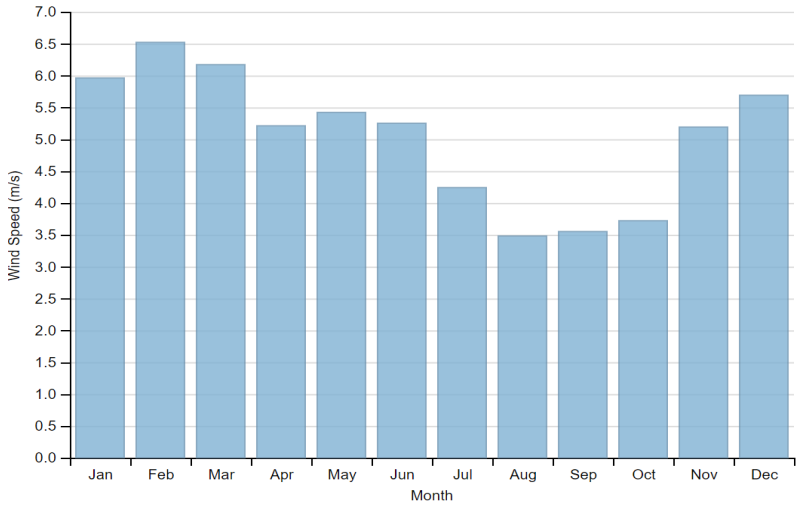


Figure 6. The average monthly wind speed data in Kish Island.

3.4. Ambient Temperature

The ambient temperature significantly impacts the output of solar PV panels and the rate of exergy destruction. Consequently, ambient temperature data for Kish Island was sourced from the IrMO database [31]. A 25-year average of this data is presented in Figure 7. Notably, the average minimum temperature recorded is 19.5 °C in February, while the average maximum temperature reaches 33.5 °C in August.

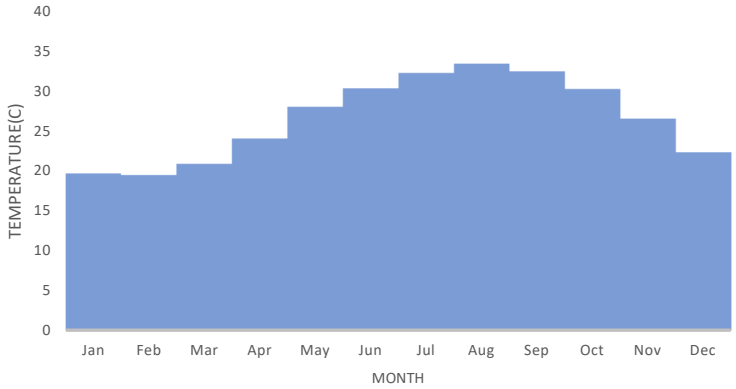


Figure 7. The average monthly ambient temperature data in Kish Island.

4. Results and Discussion

Parametric optimization using the GA was performed to determine the optimal design parameters of the MAV-CHP-HRP/BH system, aiming to minimize MTAC. Utilizing the genetic algorithm toolbox in MATLAB and considering MTAC as the objective function (along with the constraints outlined in Table 7), optimal design parameters were identified. The dynamic interfaces of both the Engineering Equations Solver (EES) and MATLAB have shown efficacy in optimizing complex systems [43]. Within our approach, the subsystems are simulated as the model converges in EES, and the optimization procedure is followed as detailed in Section 2.4. The results of this optimization process are presented in Table 8. According to the RR value in the table, the mass flowrate of the low-pressure compressor is almost three times that in the high-pressure compressor under optimum conditions. This fact indicates the significant role of the ABHP unit in reaching optimal exergy levels. This finding also aligns with the conclusions provided by Charmchi et al. [25]. PR, the second critical decision variable, is 0.68 under optimum conditions; this result demonstrates the greater role of the CHP unit in satisfying the power demand of the whole integrated system (a role more substantial than that of renewable forms of energy). The superiority of the CHP unit to the RHP/BH subsystem may be for two reasons: firstly, renewable energies are not competitive with non-renewable energies when equal weights are assigned to economic, environmental, and exergy terms in the objective function; secondly, the constant power supply of the CHP unit makes it far preferable to the erratic weather-driven power of the RHP unit.

Table 8. The quantities of decision variables under optimum conditions.

Variable	Value	Unit
RR	23	%
P_A	6.423	kPa
ΔT_{MED}	3.94	°C
T_{SS}	77.16	°C
T_{WS}	120.3	°C
PR	67	%
rp	12.7	-
$T_{in,GT}$	1055	°C
$P_{out,GT}$	192	kPa
$\dot{m}_{fuel}$	0.898	Kg/s
$T_{in,com}$	16.4	°C
N_{PV}	5734	Ea
N_{WT}	8	Ea
β_{PV}	32.4	Degrees
Ca_B	396	kWh
Ca_H	180	kWh

Considering the variation ranges of the decision variables in Table 7, the optimum values of *rp* and $T_{in,GT}$ are very close to the upper boundaries. However, the metallurgical restrictions constrain the optimization problem. Moreover, negligible share of wind turbines (N_{WT} = 8) in the optimal configuration of the RHP/BH can be attributed to the high costs of wind facilities in the case study, as summarized in Table 6. However, this number of wind turbines could produce 592.01 MWh/year of renewable electricity. The remaining 3298.4 MWh of renewable electricity was supplied by solar PVs. Considering that the literature reports the dominance of solar over wind in hybrid systems in the case study [31], this result seems acceptable. However, the size of the solar PVs and the capacity of the batteries under optimum conditions are different from those reported in the case study in the literature [31], and this fact can be attributed to the differences in the problem and solution platform between these studies. According to Figure 3, the size of the RHP/BH subsystem is determined by evaluating the power demand of the MAV unit and the optimal *PR*, whereas the HRP systems of refs. [31,42] are simulated by Blackbox HOMER and iterative LPSP algorithms. A total of 25,220.1 kg/year of green hydrogen was consumed by the fuel cells. This amount is comparable to the consumption by a fuel cell in an optimal self-scheduling system with four products [43]. The higher yield achieved with similar hydrogen consumption is mainly due to the more complex configuration of the multicarrier system and the better adaptation of reverse osmosis systems compared to MEDs for electricity usage, which were used in this study [7].

4.1. Energy, Exergy and Environmental Analyses

According to Table 8, the CHP subsystem consumes 0.898 kg/s of natural gas to provide 4.375 MW of power and 32.158 MW of non-renewable heat. All the produced heat is consumed by the MAV subsystem, but an additional HRP/BH subsystem with a capacity of 1.816 MW is required to supply the remaining needed power under optimum conditions. Because one of the key components of the MTAC is the cost of destroying the exergy of the system, it is essential to examine exergy destruction in each subsystem. Figure 8 presents the exergy destruction of each subsystem within the optimal MAV-CHP-HRP/BH system. To calculate the exergy destruction cost rate of the HRP/BH subsystem for the MTAC, the hourly exergy destroyed by the solar system, wind turbines, and energy storage systems over the course of a year is summed. We thus determined that a total input exergy of 762,872 GJ/year is destroyed within the MAV-CHP-HRP/BH system. Among the subsystems, the CHP system exhibits the highest exergy destruction at 422,409 GJ/year. Following closely, the HRP/BH and MAV subsystems contribute to exergy destruction with rates of 197,068 GJ/year and 143,394 GJ/year, respectively. This has also been confirmed by the previous studies. The exergy analysis of a similar optimal multi-component system showed that CHP components such as the CC, GT, and AC exhibit the greatest exergy destruction among ABHP and BH facilities [12]. This result can be attributed to the transfer of heat at high temperatures alongside other irreversible processes in the CHP components. On the other hand, the MED unit destroys an average of only 13% of fuel exergy during desalination [7]. Considering the small portion of the exergy allocated to the MAV unit, it shows the best performance among the subsystems.

In accordance with the MTAC objective function outlined in Equation (42), the optimal values of TAC, exergy destruction cost, and environmental cost for each subsystem are derived to examine their respective impact on MTAC. Figure 9 illustrates the influence of each subsystem on each term of the MTAC. According to the figure, the TAC, exergy destruction cost, and environmental cost of the optimal MAV-CHP-HRP/BH system are \$29,132,075/yr, \$4,441,160/yr, and \$3,284,560/yr, respectively. Among the subsystems, MAV exhibits the highest TAC at \$19,591,900/yr, followed by CHP and HRP/BH with TACs of \$5,590,000/yr and \$3,950,175/yr, respectively. Regarding exergy destruction costs, CHP, HRP/BH, and MAV systems account for \$2,561,150/yr, \$1,088,970/yr, and \$791,040/yr, respectively. Notably, only the CHP system contributes to the environmental cost with \$3,284,000/yr. The optimal MTAC value is depicted as \$36,857,795/yr in Figure 9.

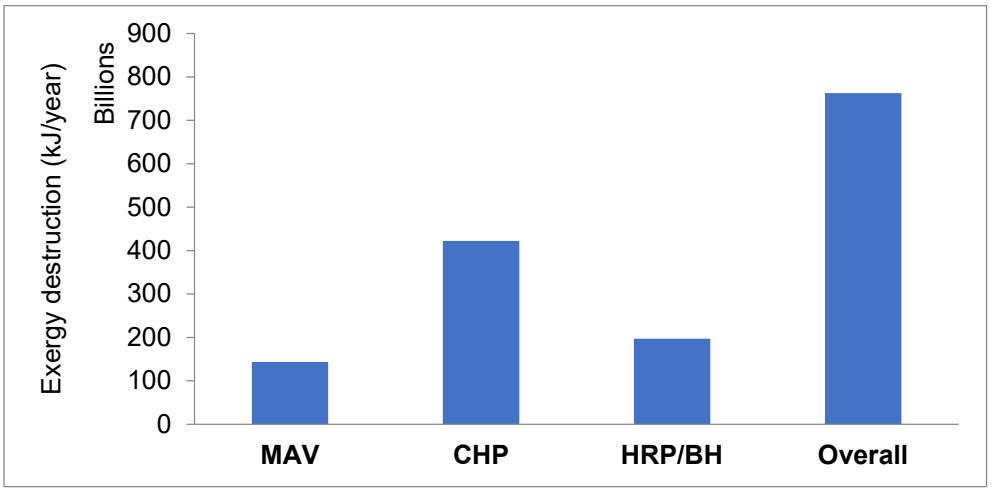


Figure 8. Exergy destruction of the subsystems.

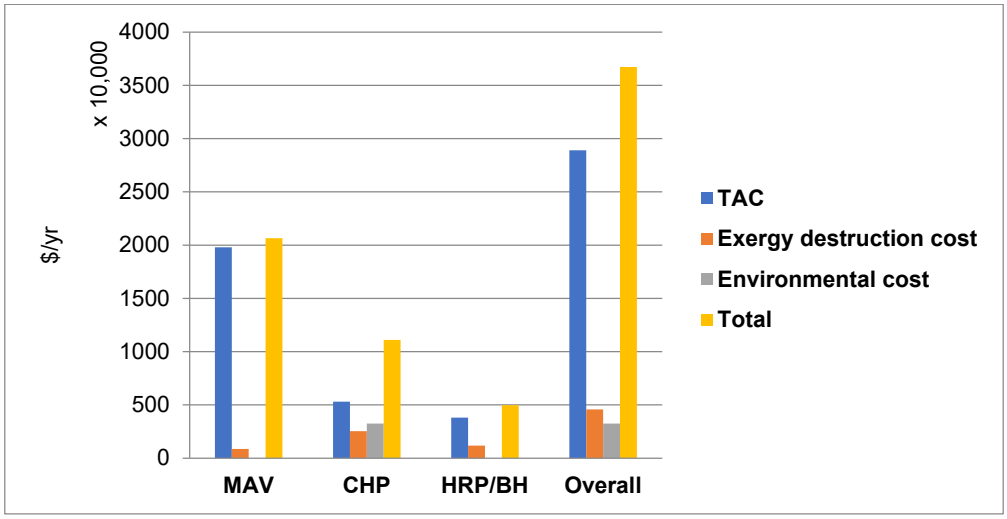


Figure 9. Effects of the subsystems on MTAC of the integrated system.

To facilitate a comparison of the significance of each subsystem's effect on MTAC, the total cost rate of each subsystem was normalized. Figure 10 illustrates the normalized cost rate for MAV, CHP, and HRP/BH. The MAV subsystem accounts for 67% of the TAC, while CHP and HRP/BH contribute 19% and 14%, respectively. In terms of exergy destruction cost rates, MAV, CHP, and HRP/BH represent 18%, 58%, and 25%, respectively. Hence, it can be inferred that MAV, CHP, and HRP/BH contribute 55%, 31%, and 14%, respectively, to the MTAC of the MAV-CHP-HRP/BH system. In Figure 11, the normalized values of TAC, exergy destruction cost rate, and environmental cost rate on MTAC are presented. TAC emerges as the dominant contributor to MTAC, accounting for 79% of the total, followed by exergy destruction cost rate and environmental cost rate (with contributions of 12% and 9%, respectively). This result is a consequence of the high replacement and maintenance costs of the RHP/BH subsystem.

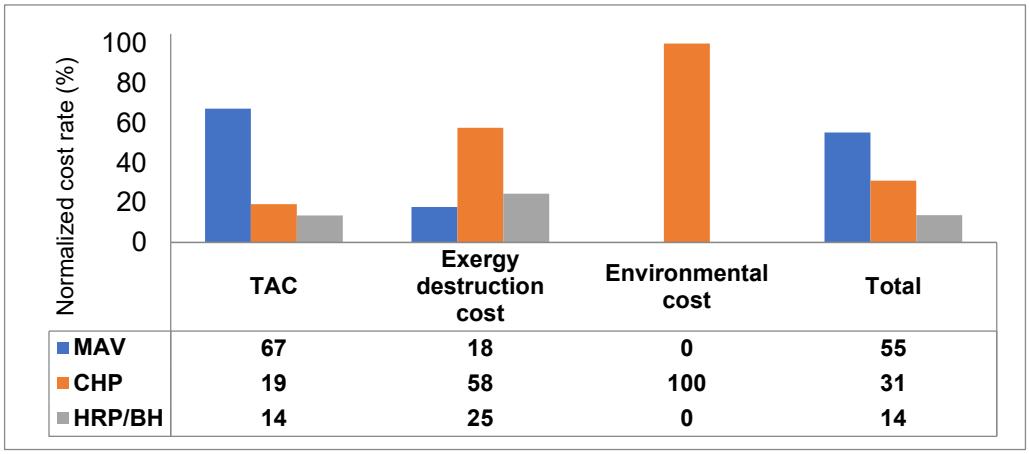


Figure 10. Normalized cost rates of each subsystem.

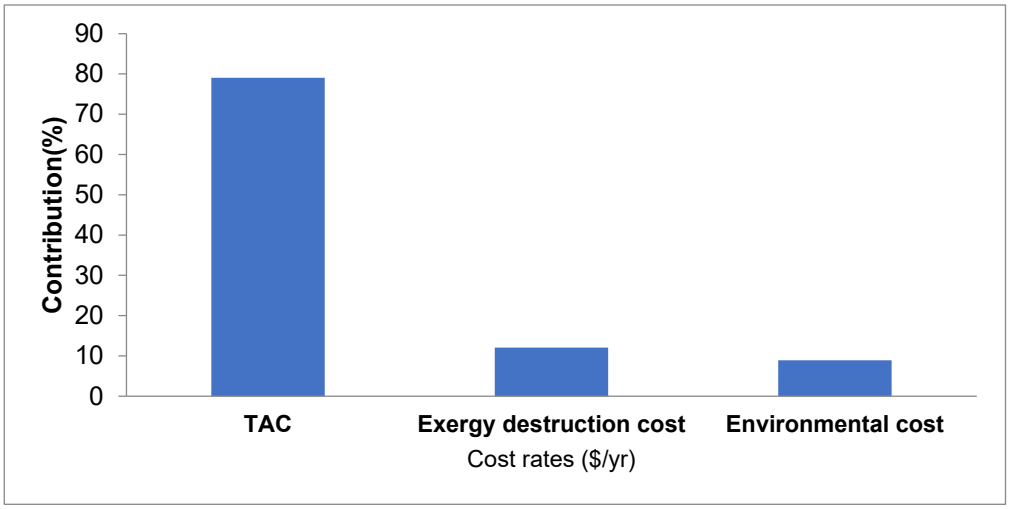


Figure 11. Normalize total annual cost, exergy destruction cost rate, and environmental cost rate.

4.2. Sensitivity Analysis

The sensitivity analysis aimed to assess how the system's MTAC responds to changes in the conditions of a given energy source, including variations in the unit price of fossil fuel, solar radiation, and wind speed. Wind power, solar radiation, and methane are the three primary energy sources of the system. Each iteration of sensitivity analysis involved repeating the optimization process while keeping other variables constant. Due to the substantial computational time required (approximately 3 h per optimization run), the sensitivity analysis was conducted only for six different energy resource scenarios, as outlined in Table 9. Different scaled annual averages of solar radiation and wind speed were utilized for this analysis. The long run of each optimal solution in a sensitivity analysis was mainly associated with the convergence of the subsystems' models rather than the optimization algorithm. This is because the hyperparameters of the GA algorithm were fixed during the sensitivity analysis.

Figure 12 illustrates the impact of the unit price of fuel on MTAC. In the graph, the red marker denotes the optimal conditions obtained while a fuel unit price of USD 0.003 per MW was in effect. The plot reveals that MTAC increases with higher unit prices of fuel, indicating a direct correlation between fuel price and MTAC. Interestingly, as fuel prices rise, their influence on MTAC diminishes, whereas their impact is more pronounced at lower prices. This trend arises because as fuel prices rise, the contribution of the HRP/BH subsystem to power generation decreases relative to the CHP system, which relies on fuel for power generation. Consequently, increased fuel prices lead to reduced fuel consumption,

thereby mitigating their effect on the MTAC of the MAV-CHP-HRP/BH system. Similar to a previous study [43], TAC is very sensitive to the CHP's fuel price when hydrogen can circulate in the system. In higher fuel prices, hydrogen facilities (i.e., the size of the corresponding HRP/BH subsystem) increase in size, which leads to an increase in total costs. It is therefore unambiguous that an increase in the unit price of fuel at greater TACs causes greater changes in the MTAC.

Table 9. Values of the uncertain variables used in the sensitivity analysis scenarios.

Unit Price of Fuel ($/MWh)	Solar Radiation (kWh/m^2/d)	Wind Speed (m/s)
3.3	4.103	3.845
6.7	5.103	4.845
10.1	6.103	5.845
13.5	7.103	6.845
16.9	8.103	7.845
20.3	9.103	8.845

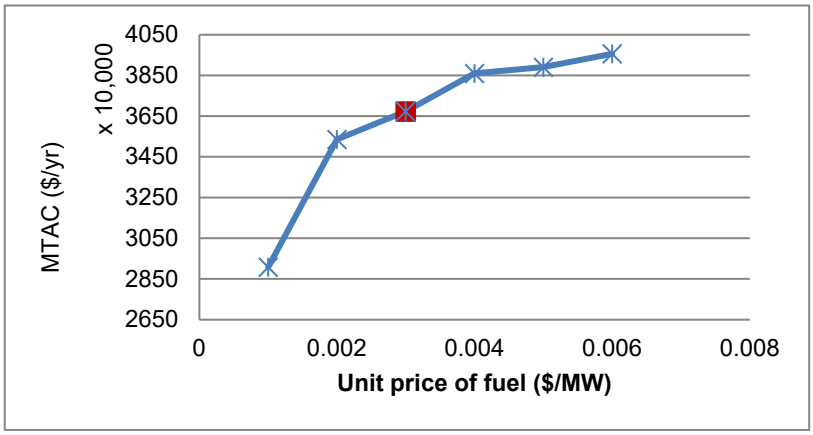


Figure 12. The impact of the unit price of fuel on MTAC in the integrated system.

Figure 13 illustrates the impact of variations in solar radiation on MTAC. The graph depicts a decrease in MTAC with increasing solar radiation. This reduction in MTAC can be attributed to the decrease in the size of the HRP/BH subsystem as solar radiation increases. Consequently, both the TAC and the exergy destruction cost of the HRP/BH subsystem decrease, leading to an overall reduction in MTAC. Interestingly, the effect of solar radiation on MTAC is more pronounced at higher values of solar radiation compared to lower values. This observation suggests that the contribution of the HRP/BH subsystem to power generation significantly increases with higher solar radiation levels, resulting in reduced fuel consumption by the CHP system. Therefore, the fuel price plays a crucial role in explaining the rapid decrease in MTAC at high solar radiation values.

Figure 14 displays the optimal values of MTAC with varying wind speeds, while keeping the fuel price fixed at 0.003 $/MW and solar radiation at 6.103 kWh/m^2.day. The graph demonstrates a decrease in MTAC as wind speed increases. This reduction in MTAC is attributed to the decrease in the size of the HRP/BH subsystem, resulting in lower TAC and exergy destruction cost for the integrated system. Interestingly, the impact of low wind speeds on MTAC appears to be more significant than that of high wind speeds. This observation suggests that the decrease in MTAC is more pronounced with lower wind speeds, possibly because the increased use of wind turbines at higher wind speeds leads to higher costs associated with the HRP/BH subsystem.

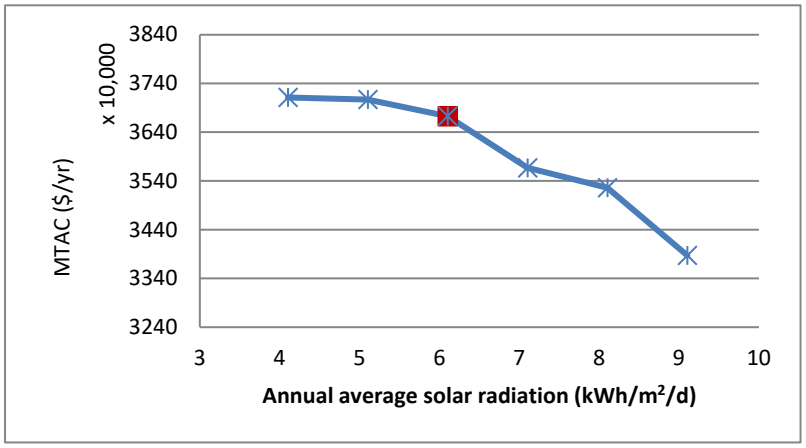


Figure 13. Effect of solar radiation on MTAC in the integrated system.

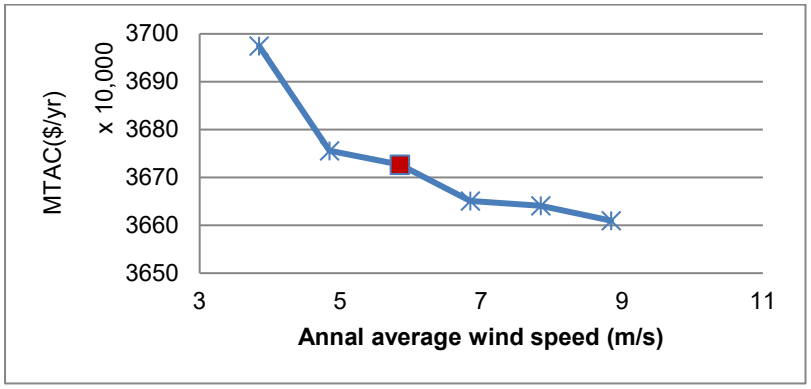


Figure 14. Effect of the wind speed on MTAC in the integrated system.

According to Equation (44), the sensitivity of the MTAC under optimum conditions was 0.22, 0.49, and 0.42, with respect to the fuel price, solar radiation, and wind speed, respectively. This indicates that solar radiation has the most significant impact on optimum MTAC and should be given greater consideration during the operation of the optimal combined system. Moreover, the proposed iterative thermo-econo-environmental modeling platform (Figure 2) prioritizes the MAV simulation, modeling the other subsystems based on the key values of *RR* and heat demand of the MAV at the model's converged solutions. Consequently, the optimization model exhibits heightened sensitivity to the MAV decision variables compared to the parameters of the other subsystems. Future research should develop non-parametric iterative models that ensure equal sensitivity to the parameters of all subsystems.

5. Conclusions

In this study, we developed an integrated system comprising MAV, CHP, and HRP/BH subsystems to optimize freshwater and cooling cogeneration. By leveraging the cooling effect of the MAV subsystem's evaporator, we aimed to enhance overall system performance. Validating our thermo-econo-environmental model in Kish Island, we targeted a peak production rate of 15,000 m^3/d freshwater and 30,000 kW cooling by minimizing the modified total annual cost (MTAC). The following are the key conclusions drawn under optimal conditions:

- Cooling the gas turbine inflow through internal heat recovery boosted the efficiency of the CHP, enabling it to supply 4.375 MW of the required electricity and all the necessary heat (32.158 MW). However, including the environmental costs in the proposed objective function (MTAC) led to the green HRP/BH subsystem supplying the remaining 1.816 MW of the required power for the integrated system.

- The complex integration of components led to enhanced exergy and environmental performance at the expense of increased economic expenditure. Notably, the economic cost of the MAV subsystem constituted 67% of the total TAC, with only 18% of the exergy destruction costs and no contribution to environmental costs.
- Despite environmental costs representing a smaller share (9%) of the total MTAC, economic factors predominantly influenced the system's operation, contributing to 79% of total costs. Hence, future studies are recommended to assign weights to economic, exergy, and environmental terms in combined optimization objective functions.
- Our findings underscore the system's sensitivity to variations in weather-driven energy resources and how this affects fuel prices. Thus, ensuring robust system operation may require greater emphasis on fuel consumption rates, especially if newer components are to be added to the system.

The MAV was the core subsystem in the proposed iterative thermo-econo-environmental model, which limited the impact of changes in the parameters of other subsystems on the objective function. Future research could extend this study by substituting the MAV with similar desalination-refrigeration technologies, validating the system in environments with lower solar radiation and greater seawater salinity, and considering variations in product prices to provide further insights into system dynamics.

Author Contributions: Conceptualization, I.J.E.; methodology, I.J.E.; software, I.J.E.; validation, I.J.E. and P.I.; formal analysis, I.J.E.; investigation, I.J.E.; resources, I.J.E.; data curation, I.J.E.; writing—original draft preparation, I.J.E. and P.I.; writing—review and editing, P.I.; visualization, I.J.E. All authors have read and agreed to the published version of the manuscript.

Funding: This paper received no external funding.

Data Availability Statement: The data presented in this study are available on request from the corresponding author.

Acknowledgments: The authors would like to convey their sincere appreciation to Glopex (https://glopex.kr/, accessed on 8 May 2023). We would also like to thank our coworkers/collaborators for their suggestions in improving the paper. We also thank the editorial staff and reviewers for their insightful criticism and recommendations, which considerably raised the quality of this work. We warmly thank Glopex for their dedication to science and their conviction that this research is crucial.

Conflicts of Interest: Iman Janghorban Esfahani was employed by the Glopex Co., Ltd. The other author declares that the research was conducted in the absence of any commercial or financial relationships that could be construed as a potential conflict of interest.

Abbreviations

The nomenclature is given as the abbreviations, variables and their corresponding units, subscripts and superscripts in this section.

Abbreviations			
Multi-effect distillation	MED	Modified extended power pinch analysis	MEPoPa
Multi-stage flash	MSF	Standard test conditions	STC
Gas turbine	GT	Proton exchange membrane fuel cell	PEMFC
Absorption heat pump	ABHP	Combustion chamber	CC
Vapor compression refrigeration	VCR	Generator	G
MED-ABHP-VCR subsystem	MAV	Direct current	DC
Hybrid renewable power	HRP	Solar photovoltaic	PV
Combined heat and power	CHP	Total annual cost	TAC
Expansion valve	EV	Heat recovery steam generator	HRSG
Battery and hydrogen	BH	Air compressor	AC
Solution heat exchanger	SHX	Iran Meteorological Organization	IrMO
Variables			
Modified total annual cost ($\$\cdot year^{-1}$)	MTAC	Air fuel ratio ($kg\cdot kg^{-1}$)	AFR
Annual operational cost ($\$\cdot year^{-1}$)	*AOC*	Power output of PV under STC (kW)	Y
Mass flow rate ($kg\cdot s^{-1}$)	$\dot{m}$	Derating factor (-)	f

Solution concentration (kg·kg^{-1})	x	Temperature coefficient (K^{-1})	α
Specific enthalpy (kJ·kg^{-1})	h	Solar radiation (kW·m^{-2})	G
Heat rate (kW)	$\dot{Q}$	Solar transmittance (-)	τ
Power (kW)	$\dot{W}$	Density (kg·m^{-3})	ρ
Isentropic efficiency (-)	η	Speed (m·s^{-1})	V
Salinity (kg·m^{-3})	X	Swept area (m^2)	A
Latent heat (kJ·kg^{-1})	L	Maximum theoretical efficiency (-)	C
Temperature difference (K)	ΔT	Appropriate hydrogen tank capacity (kWh)	$AHTC$
Specific heat capacity (kJ·kg^{-1}·K^{-1})	Cp	Margin coefficient of hydrogen tank (-)	M
Temperature (K)	T	Initial pressure (kPa)	H
Heat ratio (-)	γ	Number (-)	N
Pressure (kPa)	P	Current (A)	I
Refrigerant ratio (-)	RR	Voltage (V)	V
Lower heating value (kJ·kg^{-1})	LHV	Total capital cost ($)	TCC
Exergy rate (kW)	$\dot{E}x$	Interest rate (-)	ir
Cost rate of the exergy ($·s^{-1})	$\dot{C}$	Lifetime (year)	lt
Unit cost ($·kJ^{-1})	c	Purchase equipment cost ($)	PEC
Cost rate of a component ($·s^{-1})	$\dot{Z}$	Cost ($)	C
Time (s)	t	Overall heat transfer coefficient (kW·m^{-2}·K^{-1})	U
Pressure loss (kPa)	ΔP	Area (m^2)	A
Pressure ratio (-)	rp	Capacity (kWh)	Ca
Power ratio (-)	PR	Sensitivity (-)	S
Tilt angle (rad)	β		
Subscripts and Superscripts			
Pump	Pu	Flue gas	$flue$
Brine	B	Gas turbine	GT
Feed	F	PV cell	c
Distillate	D	Reflectance	R
Number of stages	i	Direct beam	DB
Entrained steam	r	Diffuse component	DC
Condenser	Con	Ambient	a
Flash ratio	y	Maximum power	mp
Product	Pr	Solar absorptance	α
Reference	ref	Hub height	hub
Motive steam	0	Hydrogen tank	HT
Compressor	com	Actual	a
High-pressure	HP	Electrolyzer	EL
Low-pressure	LP	Fuel cell	FC
Seawater	sw	Logarithmic	lm
Power	W	Dead state	DS
heat	Q	Destruction	De
Investment			
emphI	Fuel	Fu	
Replacement	R	Loss	L
Combustion chamber	CC	Retention	r
Environmental	E	Adiabatic flame	PZ
Total	tot	Strong solution	SS
Wind turbine	WT	Absorber	A
Battery	B	Weak solution	WS
Hydrogen	H	Solar PV	PV

References

1. Raposo, V.D.B.; Costa, V.A.F.; Rodrigues, A.F. A review of recent developments on drought characterization, propagation, and influential factors. *Sci. Total Environ.* **2023**, *898*, 165550. [CrossRef]
2. Turgut, H.S.A.; Dincer, I. A microalgal biogas driven multigenerational system developed for producing power, freshwater and hydrogen. *J. Clean. Prod.* **2023**, *411*, 137341. [CrossRef]

3. Tian, C.; Su, C.; Yang, C.; Wei, X.W.; Pang, P.; Xu, J.G. Exergetic and economic evaluation of a novel integrated system for cogeneration of power and freshwater using waste heat recovery of natural gas combined cycle. *Energy* **2023**, *264*, 126227. [CrossRef]
4. dos Reis, E.P.; Arrieta, F.R.P.; Venturini, O.J. General methodology and optimization for the analysis of bottoming cycle cogeneration. *Energy Convers. Manag.* **2023**, *276*, 116536. [CrossRef]
5. Su, Z.X.; Yang, L. A novel and efficient cogeneration system of waste heat recovery integrated carbon capture and dehumidification for coal-fired power plants. *Energy Convers. Manag.* **2022**, *255*, 115358. [CrossRef]
6. de Sampaio, P.A.B.; Alves, L.F.R.; Moreira, M.D. Electricity and water cogeneration using a small PWR of 75 MW(th) coupled to a DCMD desalination plant with heat recovery. *Nucl. Eng. Des.* **2023**, *415*, 112658. [CrossRef]
7. Ifaei, P.; Charmchi, A.S.T.; Santamouris, M.; Yoo, C. Comprehensive performance evaluation of water and power production technologies using water-exergy nexus analysis. *Energy Convers. Manag.* **2023**, *284*, 116960. [CrossRef]
8. Esmaeilion, F.; Soltani, M.; Nathwani, J.; Al-Haq, A.; Dusseault, M.B. Conventional and advanced exergy and exergoeconomic analysis of a novel multi-fueled cogeneration system with desalination. *Energy Rep.* **2023**, *9*, 5704–5720. [CrossRef]
9. Pietrasanta, A.M.; Mussati, S.F.; Aguirre, P.A.; Morosuk, T.; Mussati, M.C. Optimization of Cogeneration Power-Desalination Plants. *Energies* **2022**, *15*, 8374. [CrossRef]
10. Abdulrahim, A.H.; Chung, J.N. Performance improvement of cogeneration plants in hot arid regions via sustainable turbine inlet air cooling technologies: An energy-water nexus comparative case study. *Int. J. Energy Res.* **2021**, *45*, 10765–10793. [CrossRef]
11. Dabwan, Y.N.; Zhang, L.; Pei, G. A novel inlet air cooling system to improve the performance of intercooled gas turbine combined cycle power plants in hot regions. *Energy* **2023**, *283*, 129075. [CrossRef]
12. Ifaei, P.; Charmchi, A.S.T.; Vilela, P.; Safder, U.; Yoo, C. A new utility-free circular integration approach for optimal multigeneration from biowaste streams. *Energy Convers. Manag.* **2022**, *254*, 115269. [CrossRef]
13. Khalil, M.; Dincer, I. Development and assessment of integrated hydrogen and renewable energy systems for a sustainable city. *Sustain. Cities Soc.* **2023**, *98*, 104794. [CrossRef]
14. Turgut, H.S.A.; Dincer, I. Assessment of a new binary geothermal based methanol synthesis plant with power, hydrogen and freshwater. *Energy Convers. Manag.* **2023**, *294*, 117576. [CrossRef]
15. Rodríguez, D.G.; Lira, C.A.B.D.; Lima, F.R.D.; Hernández, C.G. Exergy study of hydrogen cogeneration and seawater desalination coupled to the HTR-PM nuclear reactor. *Int. J. Hydrogen Energy* **2023**, *48*, 2483–2509. [CrossRef]
16. Al-Fadhli, F.M.; Alhajeri, N.S.; Sholapurmath, R.; Ettouney, H.; Sengupta, D.; Holtzapple, M.; El-Halwagi, M.M. Optimizing cogeneration and desalination plants by incorporating solar energy. *Desalination* **2023**, *549*, 116320. [CrossRef]
17. Hoettecke, L.; Schuetz, T.; Thiem, S.; Niessen, S. Technology pathways for industrial cogeneration systems: Optimal investment planning considering long-term trends. *Appl. Energy* **2022**, *324*, 119675. [CrossRef]
18. Mosaffa, A.H.; Farshi, L.G.; Khalili, S. A novel enhanced ammonia-water power/cooling cogeneration system with dual level cooling temperature: Thermodynamic and economic assessments. *Energy Convers. Manag.* **2021**, *244*, 114530. [CrossRef]
19. Sun, X.J.; Zhuang, Y.; Liu, L.L.; Dong, Y.C.; Zhang, L.; Du, J. Multi-objective optimization of heat exchange network and thermodynamic cycles integrated system for cooling and power cogeneration. *Appl. Energy* **2022**, *321*, 119366. [CrossRef]
20. Huang, J.H.; Zheng, H.F.; Kong, H. Key pathways for efficient solar thermal desalination. *Energy Convers. Manag.* **2024**, *299*, 117806. [CrossRef]
21. Shakibi, H.; Shokri, A.; Assareh, E.; Yari, M.; Lee, M. Using machine learning approaches to model and optimize a combined solar/natural gas-based power and freshwater cogeneration system. *Appl. Energy* **2023**, *333*, 120607. [CrossRef]
22. Lv, X.F.; Lv, Y.; Zhu, Y.P. Multi-variable study and MOPSO-based multi-objective optimization of a novel cogeneration plant using biomass fuel and geothermal energy: A complementary hybrid design. *Energy* **2023**, *270*, 126921. [CrossRef]
23. Mofarrah, A.N.; Jalalvand, M.; Abdolmaleki, A. Design, multi-aspect analyses, and multi-objective optimization of a biomass/geothermal-based cogeneration of power and freshwater. *Energy* **2023**, *282*, 128369. [CrossRef]
24. Jafarzad, A.; Asgari, N.; Ranjbar, F.; Mohammadkhani, F. Thermodynamic assessment and optimization of the influences of the steam-assisted turbocharging and organic Rankine cycle on the overall performance of a diesel engine-based cogeneration integrated with a reverse osmosis desalination unit. *Sustain. Energy Technol.* **2021**, *46*, 101175. [CrossRef]
25. Charmchi, A.S.T.; Ifaei, P.; Yoo, C. The nexus between water, exergy, and economics in an optimal integrated desalination system with two configurations and four operation modes. *Energy Convers. Manag.* **2022**, *251*, 114966. [CrossRef]
26. Azhar, M.U.; Anwar, M.; Khan, U.M.; Hassan, M.; Ali, S.A.M.; Waqas, A.; Somalu, M.R.; Alresheedi, F. Thermodynamic analysis of different modes of a multigeneration SOFC-CCHP system with freshwater production and LNG cold energy utilization. *Energy Convers. Manag.* **2023**, *297*, 117730. [CrossRef]
27. Huicochea, A.; Rivera, W.; Gutiérrez-Urueta, G.; Bruno, J.C.; Coronas, A. Thermodynamic analysis of a trigeneration system consisting of a micro gas turbine and a double effect absorption chiller. *Appl. Therm. Eng.* **2011**, *31*, 3347–3353. [CrossRef]
28. Yan, X.N.; Chen, G.M.; Hong, D.L.; Lin, S.R.; Tang, L.M. A novel absorption refrigeration cycle for heat sources with large temperature change. *Appl. Therm. Eng.* **2013**, *52*, 179–186. [CrossRef]
29. Yilmaz, F.; Ozturk, M.; Selbas, R. Design and thermodynamic analysis of coal-gasification assisted multigeneration system with hydrogen production and liquefaction. *Energy Convers. Manag.* **2019**, *186*, 229–240. [CrossRef]
30. Esfahani, I.J.; Kang, Y.T.; Yoo, C. A high efficient combined multi-effect evaporation-absorption heat pump and vapor-compression refrigeration part 1: Energy and economic modeling and analysis. *Energy* **2014**, *75*, 312–326. [CrossRef]

31. Ifaei, P.; Karbassi, A.R.; Jacome, G.; Yoo, C. A systematic approach of bottom-up assessment methodology for an optimal design of hybrid solar/wind energy resources—Case study at middle east region. *Energy Convers. Manag.* **2017**, *145*, 138–157. [CrossRef]
32. Zhou, K.L.; Ferreira, J.A.; de Haan, S.W.H. Optimal energy management strategy and system sizing method for stand-alone photovoltaic-hydrogen systems. *Int. J. Hydrogen Energ.* **2008**, *33*, 477–489. [CrossRef]
33. Dursun, B. Determination of the optimum hybrid renewable power generating systems for Kavakli campus of Kirklareli University, Turkey. *Renew. Sustain. Energy Rev.* **2012**, *16*, 6183–6190. [CrossRef]
34. Zoulias, E.I.; Lymberopoulos, N. Techno-economic analysis of the integration of hydrogen energy technologies in renewable energy-based stand-alone power systems. *Renew. Energy* **2007**, *32*, 680–696. [CrossRef]
35. Li, Q.; Moya, W.; Esfahani, I.J.; Rashidi, J.; Yoo, C. Integration of reverse osmosis desalination with hybrid renewable energy sources and battery storage using electricity supply and demand-driven power pinch analysis. *Process Saf. Environ.* **2017**, *111*, 795–809. [CrossRef]
36. Fu, C.; Wang, J.J.; Shen, Q.F.; Cui, Z.H.; Ding, S. Determining the optimal biomass-gasification-based fuel cell trigeneration system in exergy-based cost and carbon footprint method considering energy level. *Energy Convers. Manag.* **2024**, *299*, 117802. [CrossRef]
37. Dincer, I.; Colpan, C.O.; Ezan, M.A. *Environmentally-Benign Energy Solutions*, 1st ed.; Springer: Cham, Switzerland, 2020.
38. Ahmadi, P.; Dincer, I. Thermodynamic and exergoenvironmental analyses, and multi-objective optimization of a gas turbine power plant. *Appl. Therm. Eng.* **2011**, *31*, 2529–2540. [CrossRef]
39. Nazari-Heris, M.; Mohammadi-Ivatloo, B.; Gharehpetian, G.B. A comprehensive review of heuristic optimization algorithms for optimal combined heat and power dispatch from economic and environmental perspectives. *Renew. Sustain. Energy Rev.* **2018**, *81*, 2128–2143. [CrossRef]
40. Hesamfar, F.; Ketabchi, H.; Ebadi, T. Multi-dimensional management framework on fresh groundwater lens of Kish Island in the Persian Gulf, Iran. *J. Environ. Manag.* **2023**, *347*, 119032. [CrossRef]
41. Mohamadi, S.; Madadi, R.; Rakib, M.R.J.; De-la-Torre, G.E.; Idris, A.M. Abundance and characterization of personal protective equipment (PPE) polluting Kish Island, Persian Gulf. *Sci. Total Environ.* **2023**, *854*, 158678. [CrossRef]
42. Fazelpour, F.; Soltani, N.; Rosen, M.A. Feasibility of satisfying electrical energy needs with hybrid systems for a medium-size hotel on Kish Island, Iran. *Energy* **2014**, *73*, 856–865. [CrossRef]
43. Ba-Alawi, A.H.; Ifaei, P.; Yoo, C. Reliable operation of an optimal self-scheduling multicarrier system with two alternatives: Multiple renewable utilities or hydrogen facilities. *J. Clean. Prod.* **2023**, *420*, 138463. [CrossRef]

Disclaimer/Publisher's Note: The statements, opinions and data contained in all publications are solely those of the individual author(s) and contributor(s) and not of MDPI and/or the editor(s). MDPI and/or the editor(s) disclaim responsibility for any injury to people or property resulting from any ideas, methods, instructions or products referred to in the content.